Journal of Biomedical Materials Research Part A

# Synthesis and characterization of biomimetic bioceramic nanoparticles with optimized physicochemical properties for bone tissue engineering

| | |
|---|---|
| Journal: | *Journal of Biomedical Materials Research: Part A* |
| Manuscript ID | Draft |
| Wiley - Manuscript type: | Original Article |
| Date Submitted by the Author: | n/a |
| Complete List of Authors: | ebrahimi, mehdi; Prince Philip Dental Hospital, Prosthodontics<br>Botelho, Michael; Prince Philip Dental Hospital, Prosthodontics<br>Lu, William; University of Hong Kong Li Ka Shing Faculty of Medicine, Orthopaedics and Traumatology<br>Monmaturapoj, Naruporn; National Metal and Materials Technology Center (MTEC), Polymer unit |
| Keywords: | Nanoparticle, Bioceramics, Biphasic calcium phosphate, Biomimetic, Bone tissue engineering |
| | |

# Synthesis and characterization of biomimetic bioceramic nanoparticles with optimized physicochemical properties for bone tissue engineering

Mehdi Ebrahimi [1*], Michael Botelho [1*], William Lu [2], Naruporn Monmaturapoj [3]

[1] Prosthodontics, Prince Philip Dental Hospital, The University of Hong Kong, Hong Kong
[2] Orthopaedics and Traumatology, Li Ka Shing Faculty of Medicine, The University of Hong Kong, Hong Kong
[3] National Metal and Materials Technology Center (MTEC), NSTDA, Thailand

*Corresponding authors: Prince Philip Dental Hospital, 34 hospital road, Sai Ying Pun, Hong Kong

## Abstract

Calcium phosphate bioceramics nanoparticles such as nano hydroxyapatite (nHA) and nano tricalcium phosphate (nTCP) are the main focus of basic and applied research for bone tissue regeneration. In particular, a combination of these two phases (nHA + nTCP) which refers to as "nano biphasic calcium phosphates (nBCP)" is of interest due to the preferred biodegradation nature compared to single-phase bioceramics. However, the available synthesis processes are challenging and the biomaterials properties are yet to be optimized to mimic the physiochemical properties of the natural nanoscale bone apatite. In this study, a new approach was developed for the production of optimized bioceramic nanoparticles aiming to improve their biomimecity for better biological performances. Nanoparticles were synthesized through a carefully controlled and modified wet mechano-chemical method combined with a controlled solid state synthesis. Different processing variables have been analyzed including; milling parameters, post-synthesis treatment, and calcination phase. Detailed physicochemical characterizations of nanoparticles revealed higher crystallinity (~100%), lower crystallite/particle size (58 nm), higher homogeneity, reduced particle agglomeration size (6 µm), and a closer molar ratio (1.8) to biological apatite compared to control and standard samples. Furthermore, the study group was confirmed as calcium-deficient carbonate-substituted BCP nanoparticles (nHA/nβ-TCP: 92/8 %). As such, the introduced method can afford an easier and accurate control over nanoparticle physiochemical properties including the composition phase which can be used for better customization of biomaterials for clinical applications. The findings of this paper will also help researchers in the further advancement of production strategies of biomaterials.

**Keywords**: Nanoparticle, Bioceramics, Biphasic calcium phosphate, Biomimetic, Bone tissue engineering.

## Introduction

**Bioceramic nanoparticles** such as nano-hydroxyapatite (nHA) and nano-tricalcium phosphates (nTCP) have gained particular interest in bone tissue engineering because of their similarity to natural bone structure and advantageous properties including distinctive biological behaviors, successful clinical history, and greater demand and expectations in the surgical field [1]–[3]. Currently, these materials are widely used as implant coating and bone substitutes in traumatology, orthopedic, maxillofacial, and dental surgery applications. As such, improvement of synthesis methods and biomaterials properties is the interest of many studies. The physiochemical properties of biomaterials are known to influence the ion-exchange, protein adsorption, cellular behavior, mechanical properties, and biodegradation rate that in turn determine the overall bioactivity and clinical performances of biomaterials [4].

To that end, **different synthesis methods** have been introduced using a wide range of precursor raw materials (e.g., $CaHPO_4$, $Ca_2P_2O_7$, $CaCO_3$, CaO, $Ca(OH)_2$, *etc.*) [5]. The synthesis methods include; precipitation and co-precipitation, sol-gel techniques, hydrothermal synthesis, mechano-chemical, plasma spray process, microwave sintering, hydrolysis, and laser-induced techniques [6],[7]. Among these, the sol-gel, co-precipitation and mechano-chemical methods have been used widely for production of nHA [8]. However, the complexity of synthesis procedure, high cost, poor reproducibility, difficult control of processing variables, low-yield end product, and high byproducts are common technical challenges during synthesis methods [9],[10]. Moreover, the produced nHA does not really mimic the detailed physicochemical properties of biological HA. For instance, these nanoparticles often suffer from several shortcomings such as non-homogeneous distribution pattern and high agglomeration rate which induce the potential heterogeneity of biological responses [9],[11]. Moreover, the poor crystallinity and low biodegradation rate are reported to result in unpredictable bioactivity [9],[11].

Introduction of biphasic bioceramics could partially overcome the limitations of single phase biomaterials by improving the biocompatibility and bioactivity. Here, nHA is usually combined with other phases (i.e., TCP) of a higher biodegradation rate to overcome its poor biodegradation rate that may interfere with bone regeneration and remodeling [12]. We have reported earlier on the synthesis of bioceramic nanoparticles (e.g., HA, β-TCP, and BCP) where the in vitro biological performances of different BCP ratios were studied concluding that the particle properties such as particle size and microtopography are more influential than the composition ratios [13]–[15]. Further comprehensive reviews on BCP are also available where we summarized all necessary details from the literature for reference [12],[16]. However, the available production methods of bioceramics nanoparticles, in

particular, BCP still encounter critical challenges in controlling the detailed physiochemical properties of nanoparticles as well as the composition phases of biomaterials [12].

Therefore, the attempt of the current study is to further optimize the biomaterials physicochemical properties by improving the manufacturing process considering the biomimetic strategies as well as economic, ecologic, and environmental factors [11],[17]. Different biomaterial processing aspects aspect were explored to mimic the exact physicochemical features of biological apatite which is non-stoichiometric, carbonate-substituted, and calcium-deficient nHA [17]–[19]. This increased biomimecity is expected to improve the bioactivity and clinical performances of nanoparticles.

This study explored a novel synthetic approach based on the conventional wet mechano-chemical method which is a simple, low-cost, low temperature, high-yield end-product method for bulk synthesis of pure nanoparticles with no byproducts. However, the size of the produced nanoparticles is reported to be usually large with poor homogeneity pattern and poor crystallinity [5],[20]. To overcome these limitations, several modifications were introduced in manufacturing parameters during the wet mechano-chemical method for an accurate control of production variables. Furthermore, this method was combined with the solid-state synthesis method for further optimization of nanoparticles through control of their crystallinity, homogeneity, and thermal behavior [5],[13]. With this in mind, the following were explored in detail; control and optimization of crystal/particle size, crystallinity ratio, particle agglomeration/distribution pattern, phase purity/composition, and molar ratio. Three types of nanoparticles (two control samples and one study sample) were synthesized and then compared with a similar commercially available one (standard sample) using different physicochemical characterization technique.

## Materials and Method

### Synthesis of nanoparticles

Pure nHA-2 powder (study sample) was synthesized using a modified wet mechano-chemical synthesis technique and solid-state reaction based on a technique from our previous reports [13],[14]. For comparison purposes, two other bioceramic powders were also synthesized as control samples; nHA-1 which was produced according to our last synthetic method [13],[14], and nβ-TCP which was synthesized through a modified method (Table 1). Moreover, a commercial nHA-F (Fluidinova®, nanoXIM•HAp202) was purchased as a standard sample based on their similar particle/crystal size to nHA-2. For the synthesis of bioceramics, the initial raw powders of calcium carbonate ($CaCO_3$, Carlo Erba Reagenti, Italy) and calcium phosphate dibasic ($CaHPO_4$, Sigma-Aldrich, Germany) were used as received, then mixed and milled in a high density polyethylene bottle (250 ml) with zirconia

milling balls (30% of bottle volume) at room temperature. Nano hydroxyapatite (nHA) was synthesized using the $CaHPO_4$ : $CaCO_3$ at a ratio of 1.5:1 [21]. The chemical reaction is as follow:

$$4CaCO_3 + 6CaHPO_4 \rightarrow Ca_{10}(PO_4)_6(OH)_2 + 2H_2O + 4CO_2 \quad (1)$$

For the synthesis of nano beta-tricalcium phosphate (nβ-TCP), the initial $CaHPO_4$: $CaCO_3$ powders were mixed at a ratio of 2:1 [21]. The equation is as follow:

$$CaCO_3 + 2CaHPO_4 \rightarrow Ca_3(PO4)_2 + H_2O + CO_2 \quad (2)$$

The modified synthesis method was applied by using smaller and more uniform zirconia milling balls (3 mm), increasing the percentage of the aqueous medium, and increasing the total milling time. Briefly, for nHA-2 the initial milling of raw powders was performed at 170 rpm rotation speed for 24 hours (Table 1). The obtained slurries after ball milling were dried in a hot oven overnight at 70 °C, bulk grounded and exposed to secondary milling for another 29 hours. Then, the slurry was dried again and the obtained powders were ground and sieved using the double-sieve technique (106 and 25 µm) for further refinement. Later, the powders were heat treated using a controlled calcination program at 900 °C for 1 hour using scientific furnace (Lenton, UK) at a heating rate of 300 °C / hour.

**Characterizations of nanoparticles**

***X-ray diffractometry (XRD)***

Crystallography of nanoparticle powders was performed by an X-ray diffractometer (X'pert PRO, PANalytical, Netherland) using Cu radiation ($\lambda$=0.15405 nm) operated at 40 KV and 35 mA in continuous scan mode with step size 0.02° from 10° to 60° (2θ) at a scan speed of 0.04 °/s. The XRD spectra were analyzed using JADE software and ICDD standard (JCPDS card no. 09-0432 for pure HA and card no. 09-0169 for pure β-TCP). Analysis of crystal size and the crystalline/amorphous phases was performed by the study of samples using "TOPAS" software (version: 4.2, Bruker, Mannheim, Germany).

***Particle size analysis (PSA)***

The particle size and the particle size distribution pattern were studied by laser diffraction technique (Mastersizer 2000, Malvern Instruments, UK) coupled with Malvern software. Briefly, the powder was dispersed in DI water followed by 4 minutes of ultrasonic bath treatment. Adequate sample concentration with the obscuration range of 10-30 % was used and exposed to stirring at 2000 rpm during analysis. Each sample analyzed in triplicate, and the results were expressed in average.

### *Scanning Electron Microscopy (SEM)*

Microstructural and morphological study of nanoparticle powders (i.e., size, shape, and agglomeration pattern) was performed using SEM. All samples were sputter coated (JEOL, JFC-1200, Japan) with Au under vacuum and observed using SEM (JEOL, JSM-7800F Prime, Field Emission SEM, Japan).

### Energy Dispersive Spectroscopy (EDS)

The elemental composition of the nanoparticles was analyzed using SEM (Hitachi, SU1510, Japan) coupled with energy dispersive X-ray spectroscopy (IXRF system, 550i analyzer, US). The Spectrometer was operated at 15 KV with a sampling depth of 1-2 μm and a resolution of 1 $\mu m^2$. Average of 3 wide scan areas was used for calculation of mean elemental composition.

### *Fourier Transform Infrared Spectrophotometry (FTIR)*

FTIR was performed (Spectrum One FTIR spectrometer, Perkin Elmer, US) to investigate the functional biochemical groups of nanoparticles. For sample preparation, the nanoparticles (1.5 mg) were milled together with potassium bromide (KBr, 100 mg) followed by compression under a hydraulic pressure (ASTM E1252-98). FTIR spectrophotometry was done using middle range infrared over a frequency region of 4000-400 wave number $cm^{-1}$ at a resolution of 4 $cm^{-1}$.

### *Thermogravimetric analysis (TGA)*

The thermal behavior of nanoparticles was studied by monitoring the mass changes of the nanoparticles as a percentage of weight over a specified temperature program in a controlled atmosphere. A 5-10 mg sample of the powder was analyzed using thermal analyzer instrument (Mettler Toledo AG, TGA/SDTA851e, Switzerland) in a temperature range of 30 °C to 600 °C with a heating rate of 10 °C/ min.

### *Statistical analysis*

Statistical analysis was done using SPSS software (SPSS ver. 24, Chicago, IL). All results were represented in the form of mean ± SD. Independent Student's t-test (two-tailed) was applied to analyze statistical significance with the p-value $< 0.05$.

## Results

### *Crystallography and phase analysis*

XRD pattern of nHA powders (nHA-2, nHA-1, and nHA-F) indexed major characteristic peaks (positions and intensities) consistent with ICDD standard for HA (JCPDS no. 09-0432). Presence of nHA phases was confirmed by detecting main Miller indices (hkl) of the diffraction peaks (peak position) at 2-Theta diffraction angles. The main diffraction peaks of HA can be reported using $d_{hkl}$

and relative intensity as follow ($d_{hkl}$ / relative intensity): (002)/42%, (211)/100%, (112)/56%, (300)/62% , (202)/28% , (130)/22%, (222)/30%, and (213)/35% (Fig. 1) [22]. Similarly, for nβ-TCP powder, major characteristic peaks of pure β-TCP were detected corresponding to ICDD standard (JCPDS no. 09-0169) (Fig. 2). However, further study of XRD pattern revealed two minor peaks attributed to β-TCP - $Ca_3(PO_4)_2$ - that were detected only in nHA-2 sample corresponding to Miller indices (hkl); (0,2,10) and (0,1,14) (Fig. 1). Overlapping and comparing XRD patterns revealed narrower peaks of higher intensities in synthesized nHA-2 and nHA-1 when compared with commercial nHA-F that exhibited broader peaks of lower intensities (Fig. 2). Both nHA-1 and nHA-2 expressed similar pattern with minor differences in some major peak intensities. For example, nHA-2 expressed slightly higher intensities in major peaks at Miller indices (002), (102), (210), and (130). In general, XRD diffraction peak patterns (both intensity and width) are indicators of crystallinity and crystallite size. The XRD peak broadening is mostly attributed to the decrease in crystallinity ratio, increase in the amorphous phase, and reduction of crystallite size [23]. On the other hand, the presence of narrow peaks with high intensity indicates larger crystallite size of nHA or high crystallinity with a minimum percentage of the amorphous phase (Fig. 2). The results of phase analysis and the study of crystallinity and crystal size of different powder samples are shown in Table 2 In agreement with the XRD pattern, these findings revealed the major presence of crystalline HA (92%) and a minimum presence of crystalline β-TCP (8%) in nHA-2. Therefore, nHA-2 sample is, in fact, a biphasic calcium phosphate (BCP) with HA/β-TCP composition ratio of 92/8 %. Furthermore, nHA-2 exhibited a crystallinity value of 100% with the absence of amorphous phase compared to nHA-1 (95.3% crystallinity) and nHA-F samples (77.6% crystallinity). During evaluation of the average crystal sizes of nanoparticles, nHA-F was found with the smallest crystal size (12 nm) when compared to nHA-1 and nHA-2. However, the nHA-2 crystal size was dramatically reduced when compared to nHA-1. Moreover, evaluating the main chemical formula of samples using the software program suggested that both nHA-2 and nHA-F were, in fact, calcium-deficient nHA ($Ca_{10-x}$) when compared to nHA-1.

***Functional groups characterization***

In general, the FTIR spectra of bioceramic nanoparticles displayed the typical absorption bands corresponding to the main inorganic chemical groups; $PO_4^{3-}$, $CO_3^{2-}$, $HPO_4^{2-}$, and $OH^-$ (Fig. 3 and Table 3). In particular, nHA powders revealed absorption bands similar to typical bands of the natural bone powder consisting of HA (3570, 1091, 1047, 962, 629, 601 and 570 $cm^{-1}$) with carbonates groups (1454, 1411 and 878 $cm^{-1}$) [24]. The intense absorption bands corresponding to the internal molecular vibrations of the phosphate group ($PO_4^{3-}$) were detected in all samples (Table 3). These vibrations are referred to as bending mode, symmetric and asymmetric stretch [25]. The intense absorption bands at 1047 and 963 $cm^{-1}$ correspond to $v_3$ mode (P-O) asymmetric bending and stretching and $v_1$ mode symmetric stretching vibration of $PO_4^{3-}$, respectively. The double bands at 602

and 571 $cm^{-1}$ were due to triple $v_4$ mode (O-PO) symmetric and asymmetric bending vibration of $PO_4^{3-}$ [26],[27]. Also, $v_2$ mode (O-P-O) bending vibration was detected at 473 $cm^{-1}$. The triplet bands at 1900-2050 $cm^{-1}$ of weak intensity are related to a combination of $v_3$ and $v_1$ vibration mode of $PO_4^{3-}$ [28] (Fig. 3). A minor absorption band of labile $PO_4$ was also detected at 631 $cm^{-1}$. The vibration corresponding to $CO_3^{2-}$ group was also seen at 876-878 $cm^{-1}$ ($v_2$), 1411-1422 $cm^{-1}$ and 1447-1454 $cm^{-1}$ ($v_3$) (Fig. 3). nHA-2 compared to nHA-1 showed higher intensity for $CO_3^{2-}$ peaks at 1410-1454 $cm^{-1}$, however, the peak at 878 $cm^{-1}$ was weak. Furthermore, nβ-TCP did not reveal the absorption band at 1411-1422 $cm^{-1}$ (Table 3). It should be noted that the absorption band at 878 $cm^{-1}$ may be also related to the presence of $HPO_4$ group which could partially overlap the $CO_2$ absorption band at 870-880 $cm^{-1}$ [29]. Furthermore, for nHA, additional broad absorption bands were observed related to $v_3$ and $v_1$ stretching (3000-3650 $cm^{-1}$ with a peak at 3572 $cm^{-1}$) and liberational (630 $cm^{-1}$) vibration of $OH^-$ group. Both nHA-2 and nHA-1 showed an intense absorption pattern compared to nHA-F that exhibited a broad peak. This peak was not detected in β-TCP because of the absence of $OH^-$ group in β-TCP chemical structure (Fig. 3). However, when considering the FTIR pattern of biphasic bioceramics (HA/TCP), the peaks of $OH^-$ groups can be observed corresponding to the composition ratio of HA phase. It is worth mentioning that additional peaks that indicate the presence of physically adsorbed water molecule due to moisture contamination may also be observed at 3433 $cm^{-1}$ and 1634-1650 $cm^{-1}$ referable to $v_2$ deformation mode of $H_2O$ molecules [29].

***Elemental chemical analysis***

Results of elemental surface analysis of different samples are shown in Table 4. Concentrations of major and minor elements as well as Ca/P molar ratios were calculated using atomic percentages in comparison to standard reference materials. nHA-2 showed a lower Ca/P molar ratio than other samples. Of particular interest was a mild reduction of zirconium ion (Zr) contamination in nHA-2 compared to nHA-1 even though it was exposed to longer milling time. The study of the impurity or trace elemental contamination showed no major difference between nHA samples.

***Particle size distribution pattern and particle agglomeration behavior***

Particle size analysis (PSA) using laser diffraction allowed the study of particle size and its distribution pattern, which is a volume-based data displayed as a frequency curve. The frequency curve can address the presence of peaks of particles and their volume-based size range distribution pattern. As such, the frequency curve can display data about the homogeneity of particle size distribution. For example, in the frequency curve, the presence of multiple peaks indicates non-homogeneity of sample size while particles with homogeneous size pattern display a single peak. Fig. 4 shows the typical results of laser diffraction technique that plots volume percentage of each sample over a range of particle diameters suspended in DI water. nHA-1 sample exhibited a curve of the bimodal peak which denotes a bimodal particle size distribution of a lower homogeneity, while all

other sample powders expressed monomodal pattern. The two peaks of nHA-1 were in the range of 0.6 µm to 9.3 µm, and 9.3 µm to 126 µm. This means that there are at least two distinct sizes of particles with a higher volume mean size, 3 and 37 µm, respectively. However, nHA-2, nHA-F, and β-TCP samples displayed monomodal peak that indicates the presence of only one distinct size of particles with more homogenous distribution pattern (Fig. 4). Furthermore, as a confirmation of nanoparticles agglomeration, the laser diffraction revealed the absence of single HA crystallite as it failed to detect particle size of < 200 nm in suspension. Moreover, the study of the percentile volume distribution of nanoparticles revealed that about 88% of nHA-2, 85% of nHA-F, and 45% of the nHA-1 powders consist of a mean particle size of < 10 µm. Additional data can be found in Table 5 that shows critical nanoparticle properties measured by laser diffraction. The results are expressed as D(0.5) and D(0.9) which denote particle size at accumulated volumes of 50% and 90%, respectively, and D(4,3) which denotes the volume mean diameter. Comparing different nanoparticle samples by over-plotting confirmed a dramatic decrease in particle size of nHA-2 and an increase in specific surface area (SSA) when compared to other samples (Fig. 4).

***Morphological evaluation of nanoparticles using SEM***

SEM morphological study of samples displayed the typical tendency of nanoparticles to form clusters of particle agglomerates. For the accurate morphological study, the breakdown of agglomerates is recommended; however, the complete breakdown of agglomerates is almost impossible as it was also noted after ultrasonic bath treatments of samples [10]. Fig. 5 shows the morphological study by SEM, where clusters of agglomerated HA nanoparticles are seen consisting of fine nanocrystallites. Furthermore, the synthesized samples showed a higher tendency to agglomerate and more resistance to breakdown compared to nHA-F. The observed agglomerated particle sizes in nHA-F were about 2-5 µm, which agreed with the results of laser diffraction analysis (Fig. 5). However, the agglomerate particles in other synthesized samples exhibited a smaller size compared to nHA-F. Furthermore, nHA-2 displayed smaller and more homogeneous particle size compared to other samples (Fig. 5).

***Analysis of thermal behavior***

Results of TGA study showed that synthesized nHA samples display the most stable behavior during thermal treatment up to 600 °C with only 0.5% and 1.3% mass loss in nHA-2 and nHA-1, respectively. This was compared to nHA-F and nβ-TCP which displayed 6.5% and 2.3% mass loss, respectively (Fig. 6). For further analysis, the TGA curve of synthesized nHA was divided into two main thermal phases (Fig. 6). Phase I was characterized by an initial rapid mass loss between room temperature and 120 °C which corresponded to the evaporation of loosely bound and adsorbed water molecules due to moisture/air contamination [30]. This dehydration phase continued up to 300 °C with about 0.8% and 5.3% mass loss for nHA-1 and nHA-F, respectively, while, nHA-2 displayed no

changes. Phase II (300-600 °C) exhibited a more constant TGA curve with minor changes in the mass. The final mass residue in all samples corresponds to calcium and phosphate compounds. Similarly, it has been observed that major mass loss of HA is up to 600 °C, beyond which (up to 1200 °C) the TGA curve is stable with no significant mass loss [31]. Study of TGA patterns of different samples confirmed an improved thermal behavior with a higher thermal resistance in nHA-2 when compared to nHA-1 and nHA-F. Thermal resistance of different samples showed a decrease in the following order; nHA-2 > nHA-1 > nβ-TCP > nHA-F.

## Discussion

This study attempted to implement a biomimetic strategy to closely replicate the physicochemical properties of natural bone apatite. The biological apatite is known to be Ca-deficient, carbonate-substituted nHA with Ca/P molar ratio of approximately 1.71 and crystal size of about 50 x 30 x 2 nm [17],[32]. The introduced synthetic method is simple, reproducible, cost-effective, and environmentally friendly (green chemistry). Furthermore, it allowed proper customization of nanoparticles physicochemical properties which in turn could maximize the regenerative potentials and bioactivity of synthetic bone substitutes. To achieve the proposed aims of this study, different processing variables were carefully studied and modified from the conventional method [13],[21] including (Fig. 7);

1. Removal of auxiliary additives (e.g., solvent, dispersant, plasticizer) keeping the water the sole solvent and the only byproduct. This eliminated the need for further time-consuming purification steps [33].
2. use of smaller and more uniform milling balls,
3. increase in water percentage and total milling duration,
4. application of post-synthesis grinding using the double-sieve method, and,
5. use of controlled calcination program with a decrease in the total calcination time and final calcination temperature.

***Modification of milling parameters and their importance***

Considering the physical aspects of HA nanoparticle, the ratio of the crystalline and amorphous phase is known to affect its bone bonding ability and stability. For example, nHA with high crystallinity has exhibited a lower degradation rate, a higher shear strength, and a more stable bone integration [34],[35]. Therefore, many efforts have been made to minimize the amorphous content and increase the crystallinity ratio especially for HA coating of implant materials [35],[36]. For this purpose, milling time was one of the selected processing variables in this study to modify the crystallinity ratio. It has been reported that a prolonged milling time increases XRD peaks intensities and overall broadening corresponding to the reduction in crystallite size and increase in crystallinity ratio [5],[8] (Fig. 1 and 2). However, a prolonged ball milling time may adversely affect the degree of crystallinity [37]. In

accordance with these findings, in this study, nHA-2 was found with 100% crystallinity with the absence of amorphous content and a lower crystallite size (Table 4). Furthermore, a higher specific surface area was also detected in nHA-2 compared to other samples that should have a biological significance [4]. These properties are attributed to the proper increase of milling time in nHA-2 that allowed a higher interaction and mechanical friction between particles and milling balls which in turn resulted in higher surface defects and surface area [38]. Furthermore, modification of milling time may also influence the biomaterial properties by altering their chemical composition phase. Based on EDS study, it was found that the prolonged milling time in nHA-2 had almost no remarkable impact on major or minor elemental compositions of nanoparticles compared to nHA-1 (Table 4). This is in contrast with the literature where an increase in the milling time has been observed to increase the concentration of impurity trace elements and overall contamination [39],[40]. However, 100% pure element may not be a favorable choice as it has been reported that the availability of other elements in (i.e., Na, Mg, carbonate, F, Si) in calcium phosphates biomaterial can improve fabrication and function of bone implants when compared to pure biomaterials [32]. Furthermore, these elemental impurities can fill the defect sites in calcium-deficient nHA. Further analysis of functional groups using FTIR studies confirmed the absence of impurities and contaminations in synthesized nanoparticles which displayed absorption bands similar to the biological apatite [24] (Fig. 1 and 2). This is critical, in particular for nHA because of its smaller crystal size which renders it more sensitive to the incorporation of impurities such as nitrate, calcite, $H_2O$ and $CO_3$ into PO sites [41]. Another selected important processing variable to optimize nanoparticles was the weight percentage of the aqueous medium ($H_2O$) during ball milling. It is known that an increase in the percentage of aqueous medium influences the formation of HA phase and relevant XRD and FTIR patterns through the increase in crystallinity and the reduction in amorphous content [8]. During the synthesis of HA, the required level of hydroxyl groups should be available for effective generation of single phase HA, which is usually supplied through a dry mechano-chemical reaction between precursor powders. However, this can be accelerated by incorporation of water during milling (i.e., during wet mechano-chemical method) or an increase in water percentage as well as an increase in the milling time and milling speed. This allows an increase in the surface area of precursor powders and adsorption sites for hydroxyl groups with the generation of more HA [8]. Accordingly, in this study, the water percentage along with the total milling time was increased. This together with the selection of smaller milling balls helped to further increase the surface area and interactions at the atomic level that resulted in the elimination of undesirable secondary phases and enhanced formation of pure nHA of high crystallinity. In addition, compared to nHA-1 (99 nm), a remarkable decrease in crystal size was noted in nHA-2 (58 nm) which is almost closer to biological apatite at least from one dimension [17] (Table. 4). Furthermore, the increase in total milling time and water percentage in this study resulted in the formation of calcium-deficient nHA-2 ($Ca_{10-x}(PO_4)_{6-x}(HPO_4)_x(OH)_{2-x}$) [12]. This is attributed to

the enhancement of kinetic processes during milling that results in the ionic substitution of phosphate ions ($PO_4^{3-}$) by hydrogen phosphate ($HPO_4^{2-}$) and formation of a vacancy on $OH^-$ site [10],[42]. To further improve the quality of final synthetic products, different powder refinements and treatments have been postulated in the literature. For example, the use of some additives (i.e., water, acetone, polyvinyl alcohol, and plasticizer) has been recommended during initial ball milling to increase the homogeneity of particles. Moreover, calcination at high temperature and secondary sintering and grinding were also suggested to reduce the crystal size and homogeneity [43]. In this study post-synthesis grinding using double-sieving method was applied prior to calcination to obtain nanoparticles of higher homogeneity with smaller particle agglomerate size which is expected to allow more uniform exposure of nanoparticles to heat during calcination.

***Modification of calcination parameters and their importance***

One of the critical processing variables that modify the biomaterials properties is thermal treatment including calcination temperature, duration, and heating/ cooling rate (calcination program). It has been shown that HA synthesized at a low calcination temperature exhibit broader XRD diffraction peaks with lower intensities. An increase in calcination temperature results in narrowing and sharpening of diffraction peaks as an indicator of raised crystallinity and an increase in crystal/ grain size [44]. However, it has been reported that there is no linear relationship between temperature and crystallinity [45]. Furthermore, the thermal treatment can also induce non-structural and structural changes in the phase composition of biomaterials that can be traced as alterations in FTIR absorption bands. For example, the temperature at 500-600 °C has been reported to result in narrowing/ disappearance of adsorbed $H_2O$ bands (at 3540 $cm^{-1}$) from the spectrum (dehydration) without any impact on lattice parameters [45]. The impact of calcining temperature on structural groups has also been observed where a lower temperature (≤ 500 °C) has resulted in a broader phosphate band (at 1000 $cm^{-1}$) and absence of hydroxyl band (at 3670 and 631 $cm^{-1}$) in nHA. However, it is reported that once the calcination temperature is raised (i.e., > 700 °C) the phosphate bands become more defined, and structural $OH^-$ bands are detected because of increase in particle size [46]. Further increase in temperature leads to dehydroxylation as a result of the separation of structural $OH^-$ group with corresponding changes in absorption bands at 630 $cm^{-1}$ and 3572 $cm^{-1}$. In this study, since the calcination temperature was limited to 900 °C for a minimum possible period (1 hour), the structural $OH^-$ was preserved, and no moisture ($H_2O$) contaminations were detected as confirmed by FTIR (Fig. 3). As already highlighted, the structural change of biomaterials during the calcining process is a critical issue that affects the biomaterial phase composition and purity. In general, the high sintering temperature is applied to improve the homogeneity, crystallinity, and mechanical properties (e.g., compressive and tensile strength, toughness, stiffness) of the products [47],[48]. However, high calcination temperatures - once the temperature exceeds 900 ℃, notably if > 1200 ℃ – would increase

the chance of phase transformation and chemical decomposition of bioceramics phases [28] which result in the appearance of secondary phases [49]. Moreover, the absence of water in the sintering environment -as in this study- has been reported to increase the rate of decomposition as well as densification of HA with the corresponding decrease in grain growth [8],[10],[45]. In addition, high temperature rather than increasing the chance of decomposition, can result in coalescence of bioceramic nanoparticles with a remarkable decrease in specific surface area, increase in grain size, and decrease in porosity that would have adverse biological consequences [44],[49],[50]. However, the onset temperature at which the particle coalescence could occur was almost high in this study because of a higher Ca/P ratio [51]. Accordingly, a lower calcination temperature for a shorter period together with a proper heating/cooling rate was a proper strategy to overcome these challenges (Fig 2). This helped to minimize the risk of decomposition and control the physical properties of nanoparticles by limiting the grain growth and maintaining a high specific surface area. With regards to the phase transformation, it has been shown that the Ca-deficient HA tends to transform at a lower temperature while the stoichiometric HA (Ca/P: 1.67) is more stable (≥ 1200°C) [52]. For example, it has been reported that sintering temperature of 700 °C can result in dissociation of Ca-deficient HA into biphasic calcium phosphate compound (HA+TCP) [47]. Furthermore, FTIR study has shown that bands of β-TCP (947, 974, and 1120 $cm^{-1}$) start to show up at 900 °C with more visibility at 1200 °C along with a shift in $PO_4^{3-}$ peaks. Moreover, the corresponding bands of $CO_3^{2-}$ groups start to weaken by the temperatures exceeding 450 °C with complete disappearance at 900 °C [28]. In accordance with these findings, we observed traces of β-TCP phase in nHA-2 as a result of decomposition which transformed the nHA-2 into biphasic calcium phosphate (BCP) with HA/TCP ratio of 92/8 % (Table 4). This was attributed to Ca-deficient nature of nHA-2 and its lower Ca/P molar ratio that makes it more sensitive to decomposition at the lower calcination temperature (≤ 900 °C) [52]. However, it should be noted that the rate of this decomposition and in turn the composition ratio of HA/TCP can be controlled by modification of the calcination temperature and its duration. This would help to overcome the problem with poor biodegradation rate of nHA and to improve the biomaterials bioactivity by customizing the final product to better match each clinical requirement. The impact of calcination phase on the osteoinductivity of nanoparticles is also interesting. The literature reported a close link between osteoinductivity and thermal treatment of biomaterials through the effects on the physical particle properties, chemical phase composition, and biodegradation rate. It has been reported that bioceramics treated at a lower temperature (≤ 1100 °C) could induce earlier and higher ectopic bone formation at intra-muscular sites of animals when compared to those exposed to higher sintering temperature (≥ 1200°C) [50]. This could be due to a higher degree of porosity, roughness, and surface area that enhance the adsorption of circulating factors and cellular attachments. Furthermore, it is known that the control of composition phases of biomaterials during thermal treatment allows further

modification of the biodegradation rate and bioactivity [53], where bioceramics with more soluble phase (TCP) have been detected with higher osteoinductivity compared to less soluble phases [54],[55].

***Impacts of chemical functional groups and molar ratio***

Considering the basic chemical structure of HA ($Ca_{10}(PO_4)OH_2$), different ion substitutions are possible at various sites to be part of apatite structure; i.e. for calcium ($Zr^{2+}$, $Mg^{2+}$, $Fe^{2+}$, $Zn^{2+}$, $Na^{+}$, $Sr^{2+}$), for phosphate group ($CO_3^{2-}$, $SiO_4^{4-}$), and for hydroxyl group ($F^{-}$, $Cl^{-}$) [20]. The substituted groups provoke significant changes in the physicochemical and biological characteristics of HA crystal lattice, i.e., crystallinity, morphology, thermal behavior, and biodegradability. Therefore, to allow further optimization of nanoparticles properties, this study achieved the carbonate group substitution in HA crystal lattice as an additional step that can improve the nanoparticles biomimecity, biodegradation rate, and bioactivity. This is because the natural bone also consists of biological Ca-deficient HA with carbonate substitution [25],[29]. Furthermore, an increase in carbonate substitution is reported to enhance the biodegradation rate of biomaterials [56]. In this study, the vibrations of carbonate groups ($CO_3^{2-}$) were observed in almost all samples where nHA-2 showed the highest and nHA-F the lowest related intensity. The carbonate peaks displayed as a single peak at 878 ($v_2$ stretching mode) and doublet peaks at 1411 $cm^{-1}$ ($v_3$ symmetric stretching mode) and 1454 $cm^{-1}$ ($v_3$ asymmetric stretching mode) [57],[58]. Therefore, the corresponding peaks of carbonate group indicated carbonate substitution in the hydroxyl A-site and phosphate B-site of the HA lattice resulted in final powder as Ca-deficient HA with carbonate substitution type AB [29],[59],[60]. (Fig. 3 and Table 5). These carbonate peaks are originated from initial raw $CaCO_3$ powder, but they can also be from the solution of atmospheric $CO_2$ in the primary suspension [25],[29]. Another important parameter in control of bioactivity is the Ca/P molar ratio that should be taken into consideration. It has been reported that with increasing Ca/P molar ratios the average grain sizes, porosity %, and pore sizes reduces from microscale (at 0.5 molar ratio) to nanoscale (at 2.5 molar ratio) [61],[62]. Furthermore, lower molar ratios ( $< 1$) are shown to be improper for implantation because of their high biodegradation profile and acidic nature that can induce higher inflammation [63]. In general, higher Ca/P molar ratios (up to 2.5) have been shown to allow increased osteoblast adhesion on bioceramics [61], while other recommended Ca/P ratio of less than 2 but more than 1 to promote osteoblast viability and differentiation [62]. Therefore, considering the biomimetic strategies and available literature, this study achieved a relatively high molar ratio of newly synthesized nHA-2 (1.83) within the acceptable range and with a closer similarity to that of biological apatite (1.71) aiming better cellular support and bioactivity (Table 4) [17],[32].

***Impacts of particle distribution pattern, size range, and agglomeration size***

It is reported that increasing the particle homogeneity and reducing the particle size and size range with a subsequent decrease in agglomerate size can result in higher biocompatibility and bioactivity of

biomaterials [10],[64]. For example, homogeneity in particle size, shape or surface topography has been shown to allow a more uniform cellular behavior and tissue deposition pattern [11],[65]. Furthermore, reducing the particle size has been shown to result in an increase in specific surface area which enhances osteoblast responses to biomaterial and facilitates higher adsorption of growth factors and circulating proteins [10]. Reduction of HA particle size has also been shown to influence the nanoparticle agglomerations that in turn can modify mode and extent of nanoparticle uptake by cells and subsequent cytotoxicity. In fact, reduced HA particle size can result in a lower agglomeration rate and formation of a smaller nanoparticle agglomerate size which is linked to lower cytotoxicity and higher biocompatibility [10],[64]. Different attempts have been made for modification of particle homogeneity, size range, and agglomeration pattern. For example, it has been shown that an increase in milling time results in a rapid decrease in particle size (<1 μm) with smaller [37] and more uniform particle agglomeration [66]. Furthermore, the calcination phase has been reported to result in a reduction of particle size and size distribution range [67] and the collapse of large particle agglomerates [10]. Therefore, the current study implemented several modifications in the processing variables including; milling parameters (e.g., size/shape of milling ball and milling time), post-synthesis phase (double-sieving), and calcination program (controlled low temperature). As a result, nHA-2 was detected with reduced mean volume particle size, size range, and agglomerate size with a subsequently higher specific surface area (Fig. 4).

In summary, in this study, a novel method is introduced that addressed precise modification of processing variables with subsequent beneficial changes in physicochemical properties of nanoparticles (Table 1 and Fig. 7) as follow;

1. The calcium-deficient nature of nHA-2 nanoparticle facilitates the phase change during thermal treatment and allows the generation of nβ-TCP phase. Furthermore, the well-controlled calcination program allows further control of the composition ratio (nHA/β-TCP %) of the final products.
2. The carbonate substitution of nanoparticle enhances the biodegradation rate.
3. the achieved Ca/P molar ratio was closer to that of natural bone which can improve the biodegradation and the cellular responses.
4. The achieved lower particle size and agglomeration rate reduces the cytotoxicity and enhance the biocompatibility,
5. The higher specific surface area and homogeneity improves the protein and cellular interactions on the nanoparticle surface,
6. The higher crystallinity and lower amorphous phase improves bone bonding ability and stability, and,

7. The improved thermal behavior increases the resistance to mass loss and probably structural changes during the manufacturing process.

Therefore, the proposed synthesis method in this study can be considered an improved and alternative novel method to produce biomimetic calcium-deficient carbonate-substituted BCP (HA/TCP) bioceramic nanoparticles of a various composition ratio which in turn can control the bioactivity of biomaterials to better fulfill the clinical needs. However, the careful balance between all processing variables in this study was a critical and challenging task during the materials manufacturing process. Therefore, the findings of this study should be interpreted carefully considering the limitations of this study and other confounding factors. The optimized BCP nanoparticles in this project are been investigated further in our lab for production of composite BCP (collagen/BCP) with customized microtopography for better *in vitro* performances. Further materials processing, biological studies (e.g., *in vivo),* and industrial collaboration are being considered for proof of concept and real application of the products in the clinical fields.

## Conclusion

In this study, we have successfully applied a new synthesis approach for advanced control of physicochemical properties of nanoparticles with closer similarity to biological apatite and a possibly higher potential to maximize bone healing. Manufacturing principles such as economic, ecologic and environmental factors have also been taken into consideration. This has been achieved by careful optimization of production variables through the application of modified wet mechano-chemical method combined with controlled solid state synthesis. The biomimetic calcium-deficient carbonate-substituted biphasic bioceramic (nHA/β-TCP) nanoparticles were produced with high crystallinity and homogeneity, and lower crystallite/particle size and reduced particle agglomeration size. The calcium-deficient nature, the carbonate substitution, and β-TCP phase would improve biodegradation and release of calcium ions which in turn may contribute to osteoinductivity with earlier and higher bone regeneration. The refined nanoparticles from this proposed method can be applied individually or in combination with other polymer phases as composite scaffolds. This study provides a fundamental knowledge and an insight into the potential of improving the fabrication strategies for optimizing the nanoparticles which can be used for particular bone tissue engineering application based on the clinical requirements.

**Ethical declaration:** There was no ethical issue to declare

**Acknowledgment:** The author would like to acknowledge seed funding for basic research (HKU) and project grant of MTEC/NSTDA (Thailand) for their kind support.

## References

1. Cai Y, Liu Y, Yan W, Hu Q, Tao J, Zhang M, Shi Z, Tang R. Role of hydroxyapatite nanoparticle size in bone cell proliferation. J Mater Chem. 2007;17:3780.
2. Huang Y, Zhou G, Zheng L, Liu H, Niu X, Fan Y. Micro-/nano- sized hydroxyapatite directs differentiation of rat bone marrow derived mesenchymal stem cells towards an osteoblast lineage. Nanoscale. 2012;4:2484–90.
3. Kantharia N, Naik S, Apte S, Kheur M, Kheur S, Kale B. Nano-hydroxyapatite and its contemporary applications. J Dent Res Sci Dev. 2014;1:15.
4. Kawasaki T. Hydroxyapatite as a liquid chromatographic packing. J Chromatogr A. 1991;544:147–84.
5. Rhee S-H. Synthesis of hydroxyapatite via mechanochemical treatment. Biomaterials. 2002;23:1147–52.
6. Dorozhkin S V. Nanodimensional and Nanocrystalline Apatites and Other Calcium Orthophosphates in Biomedical Engineering, Biology and Medicine. Materials (Basel). 2009;2:1975–2045.
7. Dorozhkin S V. Nano-Sized and Nanocrystalline Calcium Orthophosphates in Biomedical Engineering. J Biomim Biomater Tissue Eng. 2009;3:59–92.
8. Kosachan N, Jaroenworaluck A, Jiemsirilers S, Jinawath S, Stevens R. Hydroxyapatite nanoparticles formed under a wet mechanochemical method. J Biomed Mater Res Part B Appl Biomater. 2017;105:679–88.
9. Supová M. Problem of hydroxyapatite dispersion in polymer matrices: a review. J Mater Sci Mater Med. 2009;20:1201–13.
10. Mostafa NY. Characterization, thermal stability and sintering of hydroxyapatite powders prepared by different routes. Mater Chem Phys. 2005;94:333–41.
11. Pan D, Wang Q, An L. Controlled synthesis of monodisperse nanocrystals by a two-phase approach without the separation of nucleation and growth processes. J Mater Chem. 2009;19:1063–73.
12. Ebrahimi M, Botelho MG, Dorozhkin SV. Biphasic calcium phosphates bioceramics (HA/TCP): Concept, physicochemical properties and the impact of standardization of study protocols in biomaterials research. Mater Sci Eng C. 2017;71:1293–312.
13. Ebrahimi M, Pripatnanont P, Monmaturapoj N, Suttapreyasri S. Fabrication and characterization of novel nano hydroxyapatite/β- tricalcium phosphate scaffolds in three different composition ratios. J Biomed Mater Res - Part A. 2012;100 A:2260–8.
14. Ebrahimi M, Monmaturapoj N, Suttapreyasri S, Pripatnanont P. The Fabricated Collagen-Based Nano-Hydroxyapatite/β-Tricalcium Phosphate Scaffolds. Adv Mater Res. 2012;506:57–60.

15. Ebrahimi M, Pripatnanont P, Suttapreyasri S, Monmaturapoj N. In vitro biocompatibility analysis of novel nano-biphasic calcium phosphate scaffolds in different composition ratios. J Biomed Mater Res B Appl Biomater. 2014;102:52–61.
16. Ebrahimi M, Botelho M. Biphasic calcium phosphates (BCP) of hydroxyapatite (HA) and tricalcium phosphate (TCP) as bone substitutes: Importance of physicochemical characterizations in biomaterials studies. Data Br. 2017;10:93–7.
17. Dorozhkin SVS V. Nanosized and nanocrystalline calcium orthophosphates. Acta Biomater. 2010;6:715–34.
18. Rey C, Combes C, Drouet C, Glimcher MJ. Bone mineral: update on chemical composition and structure. Osteoporos Int. 2009;20:1013–21.
19. Dorozhkin S V, Epple M. Biological and medical significance of calcium phosphates. Angew Chem Int Ed Engl. 2002;41:3130–46.
20. Okada M, Furuzono T. Hydroxylapatite nanoparticles: fabrication methods and medical applications. Sci Technol Adv Mater. 2012;13:064103.
21. Yang X, Wang Z. Synthesis of biphasic ceramics of hydroxyapatite and β-tricalcium phosphate with controlled phase content and porosity. J Mater Chem. 1998;8:2233–7.
22. Prevéy PS. X-Ray Diffraction Characterization of Crystallinity and Phase Composition in Plasma-Sprayed Hydroxyapatite Coatings. J Therm Spray Technol. 2000;9:369–76.
23. Nakano T, Tokumura A, Umakoshi Y, Imazato S, Ehara A, Ebisu S. Control of hydroxyapatite crystallinity by mechanical grinding method. J Mater Sci Mater Med. 2001;12:703–6.
24. Ou-Yang H, Paschalis EP, Mayo WE, Boskey AL, Mendelsohn R. Infrared microscopic imaging of bone: spatial distribution of CO3(2-). J Bone Miner Res. 2001;16:893–900.
25. Poralan GM, Gambe JE, Alcantara EM, Vequizo RM. X-ray diffraction and infrared spectroscopy analyses on the crystallinity of engineered biological hydroxyapatite for medical application. IOP Conf Ser Mater Sci Eng. 2015;79:012028.
26. Müller FA, Müller L, Caillard D, Conforto E. Preferred growth orientation of biomimetic apatite crystals. J Cryst Growth. 2007;304:464–71.
27. Koutsopoulos S. Synthesis and characterization of hydroxyapatite crystals: a review study on the analytical methods. J Biomed Mater Res. 2002;62:600–12.
28. Berzina-Cimdina L, Borodajenko N. Research of Calcium Phosphates Using Fourier Transform Infrared Spectroscopy. Infrared Spectrosc - Mater Sci Eng Technol. InTech; 2012.
29. Siva Rama Krishna D, Siddharthan A, Seshadri SK, Sampath Kumar TS. A novel route for synthesis of nanocrystalline hydroxyapatite from eggshell waste. J Mater Sci Mater Med. 2007;18:1735–43.
30. León-Mancilla BH, Araiza-Téllez MA, Flores-Flores JO, Piña-Barba MC. Physico-chemical characterization of collagen scaffolds for tissue engineering. J Appl Res Technol. 2016;14:77–

85.

31. Agrawal K, Singh G, Puri D, Prakash S. Synthesis and Characterization of Hydroxyapatite Powder by Sol-Gel Method for Biomedical Application. J Miner Mater Charact Eng. 2011;10:727–34.
32. LeGeros RZ. Calcium phosphates in oral biology and medicine. Monogr Oral Sci. 1991;15:1–201.
33. Poliakoff M. Green Chemistry: Science and Politics of Change. Science. 2002;297:807–10.
34. Nemoto R, Wang L, Aoshima M, Senna M, Ikoma T, Tanaka J. Increasing the Crystallinity of Hydroxyapatite Nanoparticles in Composites Containing Bioaffinitive Organic Polymers by Mechanical Stressing. J Am Ceram Soc. 2004;87:1014–7.
35. Xue W, Tao S, Liu X, Zheng X, Ding C. In vivo evaluation of plasma sprayed hydroxyapatite coatings having different crystallinity. Biomaterials. 2004;25:415–21.
36. Sun L, Berndt CC, Khor KA, Cheang HN, Gross KA. Surface characteristics and dissolution behavior of plasma-sprayed hydroxyapatite coating. J Biomed Mater Res. 2002;62:228–36.
37. Stingaciu M, Topole M, McGuiness P, Christensen M. Magnetic properties of ball-milled SrFe12O19 particles consolidated by Spark-Plasma Sintering. Sci Rep. 2015;5:14112.
38. Suchanek WL, Shuk P, Byrappa K, Riman RE, TenHuisen KS, Janas VF. Mechanochemical-hydrothermal synthesis of carbonated apatite powders at room temperature. Biomaterials. 2002;23:699–710.
39. Abdellatief M, Abele M, Leoni M, Scardi P. Solid State Nuclear Magnetic Resonance and X-ray Diffraction Line Profile Analysis of heavily deformed fluorite. Thin Solid Films. 2013;530:44–8.
40. Lasalvia JC, Gilde GA, Patel PJ. Effect of Hot-Pressing Conditions on the Density and Microstructure of B4C/B6Si Composites. In: Singh HL editor. 26th Annu Conf Compos Adv Ceram Mater Struct A Ceram Eng Sci Proc . Wiley; 2008.
41. Rossi AM, Prado da Silva MH, Ramirez AJ, Biggemann D, Caraballo MM, Mascarenhas YP, Eon JG, Moure GT. Structural Properties of Hydroxyapatite With Particle Size Less Than 10 Nanometers. Key Eng Mater. 2007;330–332:255–8.
42. TenHuisen KS, Brown PW. Formation of calcium-deficient hydroxyapatite from alpha-tricalcium phosphate. Biomaterials. 1998;19:2209–17.
43. Trakhtenberg IS, Rubshtein AP, Volkova EG, Petrova SA, Fishman AY, Zakharov RG, Vykhodets VB, Kurennykh TE. Effect of mechanical activation on the morphology and structure of hydroxyapatite. Inorg Mater. 2011;47:45–50.
44. LeGeros RZ, Lin S, Rohanizadeh R, Mijares D, LeGeros JP. Biphasic calcium phosphate bioceramics: preparation, properties and applications. J Mater Sci Mater Med. 2003;14:201–9.
45. Gentile P, Wilcock C, Miller C, Moorehead R, Hatton P. Process Optimisation to Control the

Physico-Chemical Characteristics of Biomimetic Nanoscale Hydroxyapatites Prepared Using Wet Chemical Precipitation. Materials (Basel). 2015;8:2297–310.

46. Mir M, Leite FL, Herrmann Junior PS de P, Pissetti FL, Rossi AM, Moreira EL, Mascarenhas YP. XRD, AFM, IR and TGA study of nanostructured hydroxyapatite. Mater Res. 2012;15:622–7.
47. Raynaud S, Champion E, Bernache-Assollant D. Calcium phosphate apatites with variable Ca/P atomic ratio II. Calcination and sintering. Biomaterials. 2002;23:1073–80.
48. Tadic D, Beckmann F, Schwarz K, Epple M. A novel method to produce hydroxyapatite objects with interconnecting porosity that avoids sintering. Biomaterials. 2004;25:3335–40.
49. Miranda P, Pajares A, Saiz E, Tomsia AP, Guiberteau F. Mechanical properties of calcium phosphate scaffolds fabricated by robocasting. J Biomed Mater Res A. 2008;85:218–27.
50. Wang L, Zhang B, Bao C, Habibovic P, Hu J, Zhang X. Ectopic Osteoid and Bone Formation by Three Calcium-Phosphate Ceramics in Rats, Rabbits and Dogs. Costa-Rodrigues J editor. PLoS One. 2014;9:e107044.
51. Bernache-Assollant D, Ababou A, Champion E, Heughebaert M. Sintering of calcium phosphate hydroxyapatite Ca10(PO4)6(OH)2 I. Calcination and particle growth. J Eur Ceram Soc. 2003;23:229–41.
52. Yoshimura M, Suda H, Okamoto K, Ioku K. Hydrothermal synthesis of biocompatible whiskers. J Mater Sci. 1994;29:3399–402.
53. Salinas AJ, Vallet-Regí M. Evolution of Ceramics with Medical Applications. Zeitschrift für Anorg und Allg Chemie. 2007;633:1762–73.
54. Chiang Y-C, Lin H-P, Chang H-H, Cheng Y-W, Tang H-Y, Yen W-C, Lin P-Y, Chang K-W, Lin C-P. A Mesoporous Silica Biomaterial for Dental Biomimetic Crystallization. ACS Nano. 2014;8:12502–13.
55. Eyckmans J, Roberts SJ, Bolander J, Schrooten J, Chen CS, Luyten FP. Mapping calcium phosphate activated gene networks as a strategy for targeted osteoinduction of human progenitors. Biomaterials. 2013;34:4612–21.
56. Kim H-W, Kim H-E, Salih V. Stimulation of osteoblast responses to biomimetic nanocomposites of gelatin-hydroxyapatite for tissue engineering scaffolds. Biomaterials. 2005;26:5221–30.
57. Chang MC, Tanaka J. FT-IR study for hydroxyapatite/collagen nanocomposite cross-linked by glutaraldehyde. Biomaterials. 2002;23:4811–8.
58. Zhai Y, Cui FZ, Wang Y. Formation of nano-hydroxyapatite on recombinant human-like collagen fibrils. Curr Appl Phys. 2005;5:429–32.
59. Merry JC, Gibson IR, Best SM, Bonfield W. Synthesis and characterization of carbonate hydroxyapatite. J Mater Sci Mater Med. 1998;9:779–83.

60. Barinov SM, Rau J V, Cesaro SN, Durisin J, Fadeeva I V, Ferro D, Medvecky L, Trionfetti G. Carbonate release from carbonated hydroxyapatite in the wide temperature range. J Mater Sci Mater Med. 2006;17:597–604.
61. Ergun C, Liu H, Webster TJ, Olcay E, Yilmaz S, Sahin FC. Increased osteoblast adhesion on nanoparticulate calcium phosphates with higher Ca/P ratios. J Biomed Mater Res A. 2008;85:236–41.
62. Liu H, Yazici H, Ergun C, Webster TJ, Bermek H. An in vitro evaluation of the Ca/P ratio for the cytocompatibility of nano-to-micron particulate calcium phosphates for bone regeneration. Acta Biomater. 2008;4:1472–9.
63. Bohner M. Calcium orthophosphates in medicine: from ceramics to calcium phosphate cements. Injury. 2000;31 Suppl 4:37–47.
64. Müller KH, Motskin M, Philpott AJ, Routh AF, Shanahan CM, Duer MJ, Skepper JN. The effect of particle agglomeration on the formation of a surface-connected compartment induced by hydroxyapatite nanoparticles in human monocyte-derived macrophages. Biomaterials. 2014;35:1074–88.
65. Murphy CM, Haugh MG, O'Brien FJ. The effect of mean pore size on cell attachment, proliferation and migration in collagen-glycosaminoglycan scaffolds for bone tissue engineering. Biomaterials. 2010;31:461–6.
66. Kim H-S, Madavali B, Hong S-J, Kim T-S. Effect of Milling Time on the Microstructure and Thermoelectric Properties of P-type TAGS-90 Alloys by HEM and SPS. Int J Appl Ceram Technol. 2016;13:239–44.
67. Thangamani N, Chinnakali K, Gnanam F. The effect of powder processing on densification, microstructure and mechanical properties of hydroxyapatite. Ceram Int. 2002;28:355–62.

## *Figure Legends*

Fig. 1. The main XRD diffraction peaks of nHA-1 and related Miller indices (hkl).

Fig. 2. XRD patterns of the synthesized nanoparticle powders. Note the differences in crystallinity between nHA-F (with broader peaks of lower intensities) and nHA-1, nHA-2, and nβ-TCP (with narrower peaks of higher intensities). Stars indicate peaks attributed to β-TCP phase.

Fig. 3. FTIR absorption patterns of nanoparticles.

Fig 4. PSA showing distribution pattern of nanoparticles in volume percentage (%). nHA-2 displays monomodal peak with reduced volume particle size compared to other samples.

Fig. 5. SEM views of nanoparticles' morphology, distribution, and agglomeration pattern.

Fig. 6. TGA of different nanoparticles during thermal exposure. nHA-2 displayed the most stable behavior with the minimum mass loss, while nHA-F showed the maximum mass loss.

Fig. 7. The synthetic method in this study and the modified processing parameters with corresponding changes in the nanoparticles.

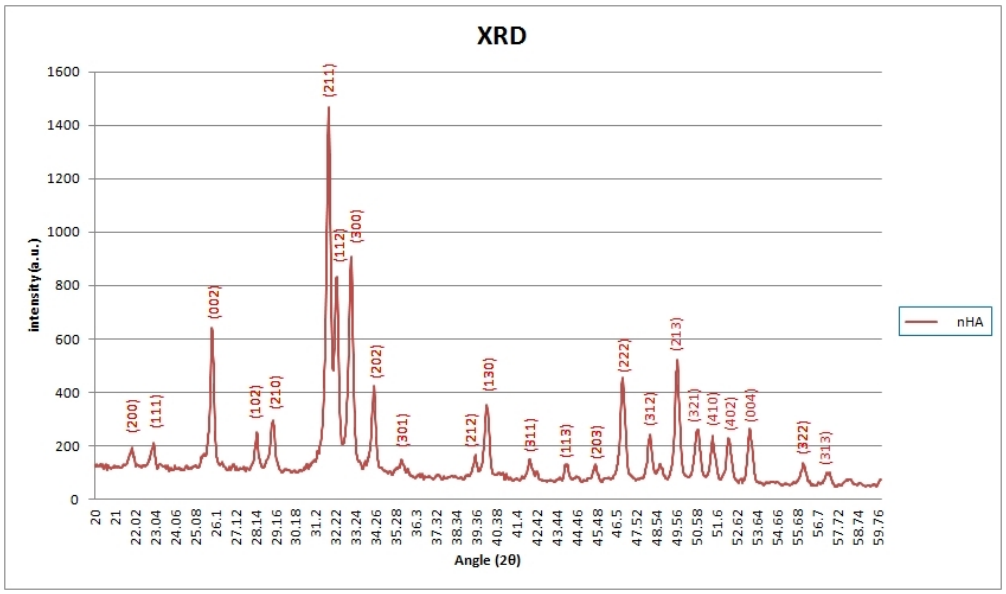


Fig. 1. The main XRD diffraction peaks of nHA-1 and related Miller indices (hkl).

297x174mm (72 x 72 DPI)

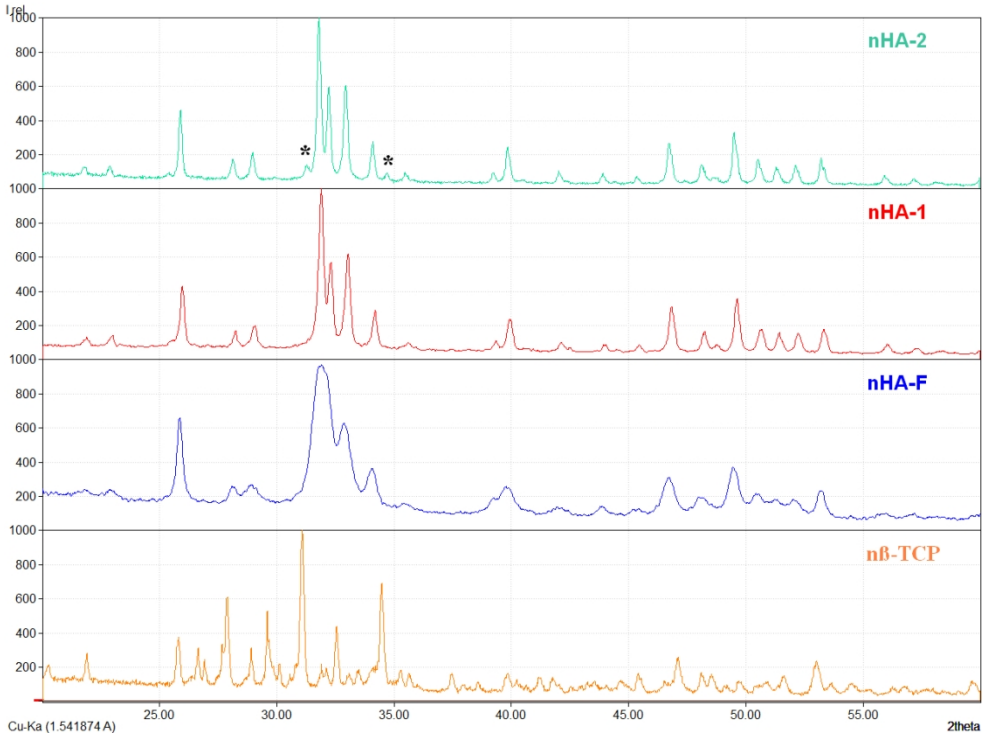


Fig. 2. XRD patterns of the synthesized nanoparticle powders.

229x167mm (144 x 144 DPI)

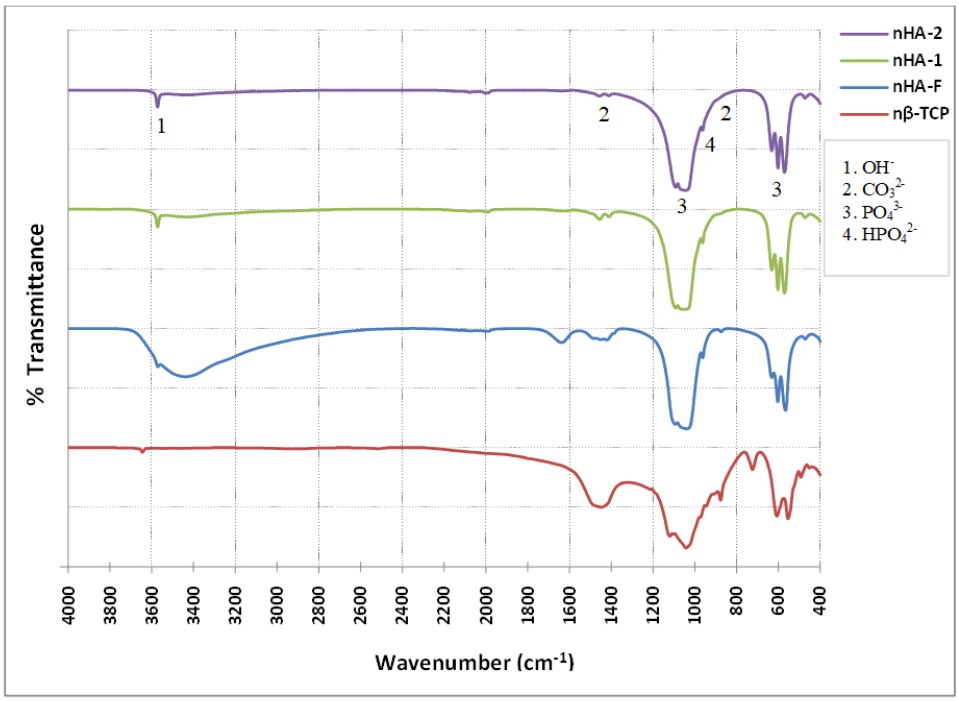


Fig. 3. FTIR absorption patterns of nanoparticles

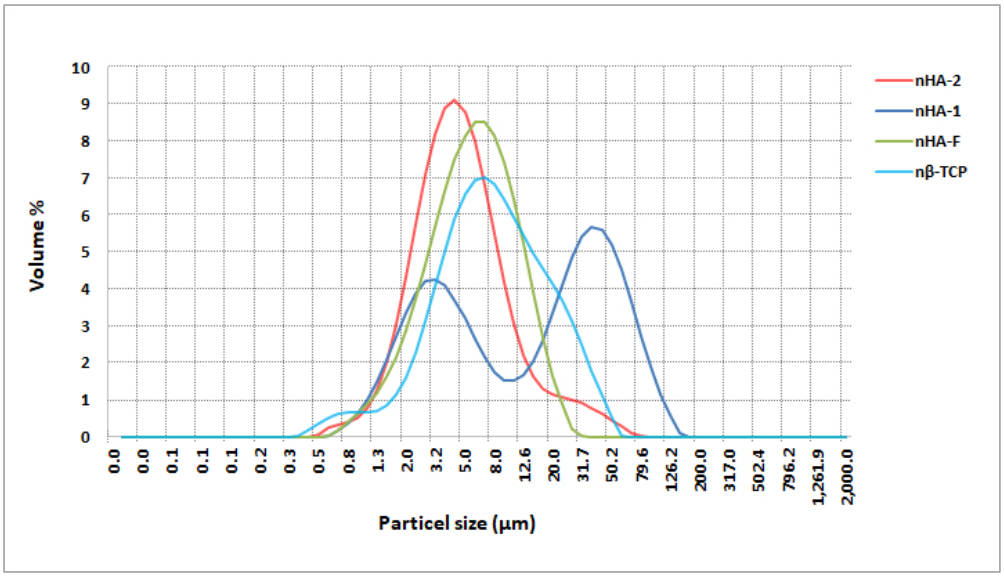


Fig 4. PSA showing distribution pattern of nanoparticles in volume percentage (%).

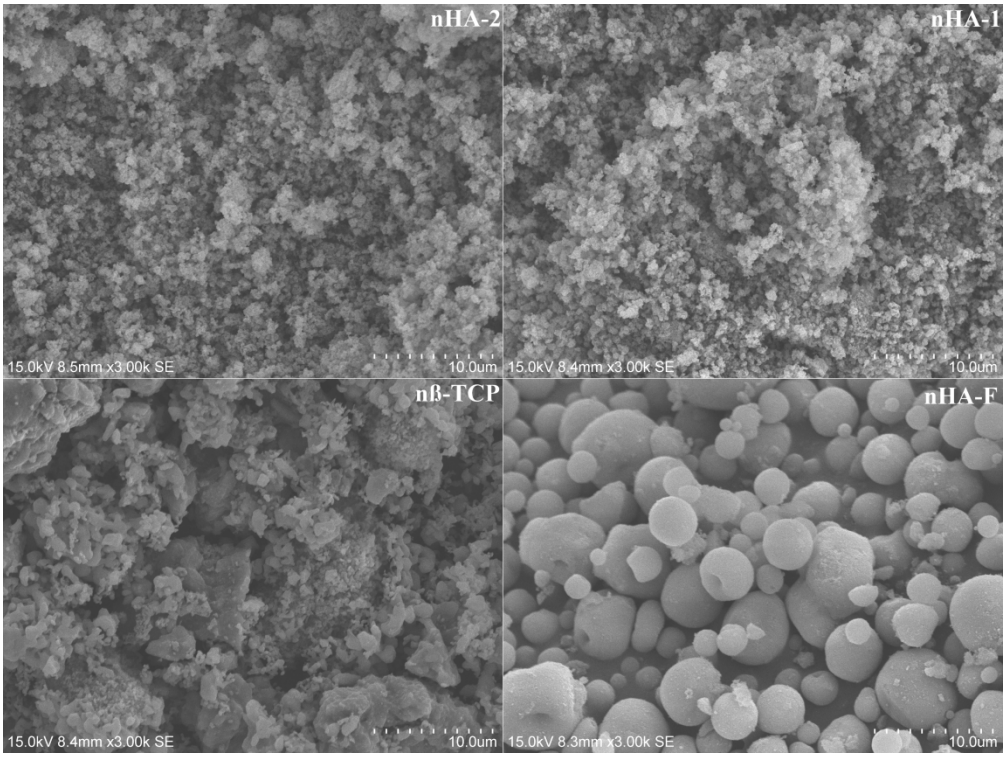


Fig. 5. SEM views of nanoparticles' morphology, distribution, and agglomeration pattern.

254x190mm (300 x 300 DPI)

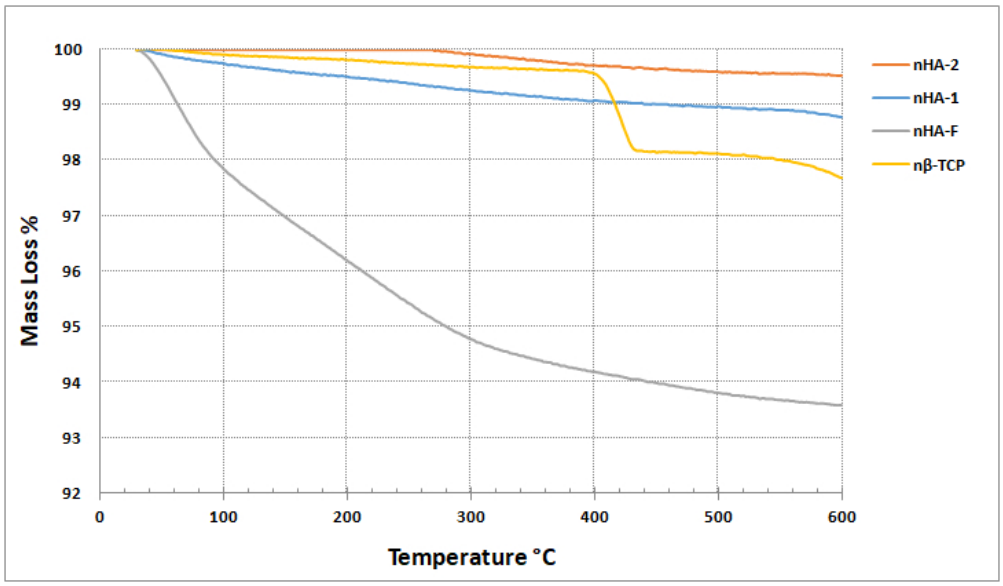


Fig. 6. TGA of different nanoparticles during thermal exposure.

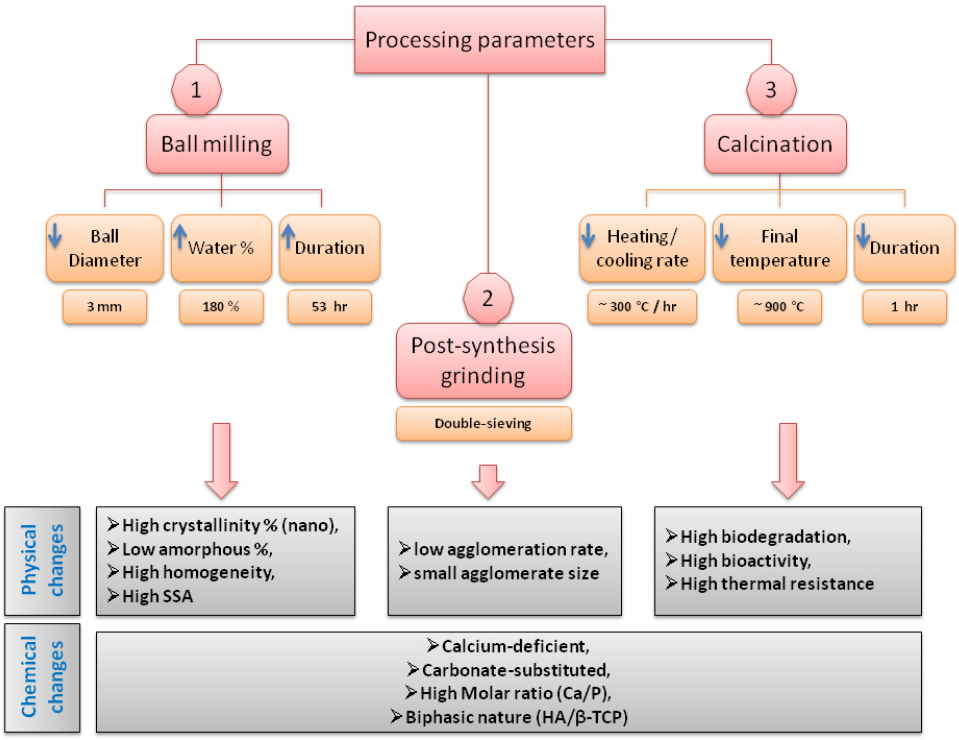


Fig. 7. The synthetic method in this study and the modified processing parameters...

254x190mm (96 x 96 DPI)

Table 1. Processing variables during synthesis of nanoparticles.

| Sample | Weight* % | Milling balls diameter (mm) | Milling time (hours) | Sieve (μm) |
|---|---|---|---|---|
| nHA-2 | 180 ($H_2O$) | Mostly 3 mm | 53 | 106 and 25 |
| nHA-1 | 130 ($H_2O$) | Mixture of 1-10 mm | 48 | 106 |
| nβ-TCP | 200 ($C_2H_6O$) | Mostly 3 mm | 29 | 106 and 25 |

* Compared to 100% (wt.) of raw powders.

Table 2. The study of chemical composition, amorphous content, crystal size, and the main chemical formula of the synthesized nanoparticles (Analysis is based on the study of XRD pattern compared to the available standard references using "TOPAS" software, version 4.2 and Match software, version 3.3.0).

| Sample ICCD # | $Ca_5(PO_4)_3OH$ 09-0432 % | $Ca_3(PO_4)_2$ 09-0169 % | $Ca_{18}Mg_2H_2(PO_4)_{14}$ 70-2064 % | $Ca_2P_2O_7$ 81-2257 % | $Ca(OH)_2$ 04-0733 % | Amorphous - % | Crystal size nm | Suggested main formula |
|---|---|---|---|---|---|---|---|---|
| **nHA-2** | 92.0 | 8.0 | 0 | - | - | 0 | 58 | $Ca_{9.6}P_{5.712}O_{26}H_2$ |
| **nHA-1** | 85.2 | 0 | 10.1 | - | - | 4.7 | 99 | $Ca_{10.0}P_{5.94}O_{27.15}H_{3.39}$ |
| **nHA-F** | 77.6 | 0 | 0 | - | - | 22.4 | 12 | $Ca_{9.6}P_{5.78}O_{26}H_2$ |
| **nβ-TCP** | - | 53.2 | - | 28.0 | 4.3 | 14.5 | 59 | $Ca_{10.1}P_7O_{28}$ |

Table 3. The main FTIR vibration bands and corresponding functional groups of nanoparticles.

| Sample | $OH^-$ | | $PO_4^{3-}$ | | | | | | $HPO_4^{2-}$ & $CO_3^{2-}$ (*V*2) | $CO_3^{2-}$ (*V*3) | |
|---|---|---|---|---|---|---|---|---|---|---|---|
| | | | *V*3 | *V*3 | *V*1 | *V*4 | *V*4 | *V*2 | | | |
| **$cm^{-1}$** | **3572** | **632** | **1091-1102** | **1042-1047** | **962-974** | **600-607** | **553-570** | **473-493** | **875-878** | **1411-1422** | **1447-1454** |
| **nHA-2** | 3572 | 632 | 1091 | 1047 | 963 | 602 | 571 | 473 | 878 | 1411 | 1456 |
| **nHA-1** | 3572 | 632 | 1091 | 1047 | 963 | 602 | 571 | 473 | 878 | 1411 | 1455 |
| **nHA-F** | 3570 | 632 | 1093 | 1043 | 962 | 603 | 566 | 473 | 875 | 1422 | 1452 |
| **nβ-TCP** | - | - | 1102 | 1043 | 974 | 607 | 554 | 492 | 876 | - | 1447 |

Table 4. Elemental chemical analysis (EDS) of nanoparticles showing the atomic percentage of the major elements and other trace elements.

| **Elements** | **nβ-TCP** | **nHA-F** | **nHA-1** | **nHA-2** |
|---|---|---|---|---|
| Ca | 31.687 | 30.911 | 30.254 | 30.033 |
| P | 14.501 | 16.102 | 14.814 | 16.343 |
| O | 38.411 | 39.456 | 38.056 | 38.408 |
| C | 6.25 | 5.729 | 7.751 | 6.984 |
| Zr | 1.387 | 1.356 | 1.331 | 1.088 |
| Al | 1.17 | 0.983 | 0.958 | 1.143 |
| Si | 1.238 | 0.968 | 0.99 | 1.176 |
| Zn | 1.092 | 0.918 | 1.651 | 1.049 |
| Mg | 1.474 | 0.889 | 1.386 | 1.321 |
| Cr | 0.597 | 0.869 | 0.78 | 0.698 |
| Na | 0.919 | 0.764 | 0.631 | 0.772 |
| Fe | 0.775 | 0.571 | 0.908 | 0.536 |
| Ag | 0.5 | 0.484 | 0.49 | 0.449 |
| **Ca/P ratio** | **2.18** | **1.91** | **2.04** | **1.83** |

Table 5. Laser diffraction study of nanoparticles showing their volume size distribution pattern.

| Sample | D (4,3) (μm) | D (0.5) (μm) | D (0.9) (μm) | SSA* ($m^2/g$) | 1st peak range (μm) | 1st peak volume % | 2nd peak range (μm) | 2nd peak volume % |
|---|---|---|---|---|---|---|---|---|
| nHA-2 | 6.3 | 4.1 | 12.1 | 1.78 | 0.5-68 | 99.9% | - | - |
| nHA-1 | 23.7 | 15.9 | 58.6 | 1.19 | 0.6-9.3 | 43% | 9.3-126 | 57% |
| nHA-F | 6.4 | 5.3 | 12.3 | 1.52 | 0.6-27 | 99.9% | - | - |
| nβ-TCP | 9.9 | 6.9 | 22.3 | 1.37 | 0.37-50 | 99.9% | - | - |

* SSA is measured as particle total area/total weight.